What Changes on the Inverse Catalyst? Insight From CO Oxidation on Au-Supported Ceria Nanoparticles Using Ab Initio Molecular Dynamics

Yong Li,[1] Shikun Li,[1] Marcus Bäumer,[1]Lyudmila V. Moskaleva,[1,2]*

1 Institute of Applied and Physical Chemistry and Center for Environmental Research and Sustainable Technology, University of Bremen, 28359 Bremen, Germany

2 Department of Chemistry, University of the Free State, PO Box 339, Bloemfontein, South Africa

[*] Corresponding author's e-mail address: lyudmila.moskaleva@gmail.com

Abstract

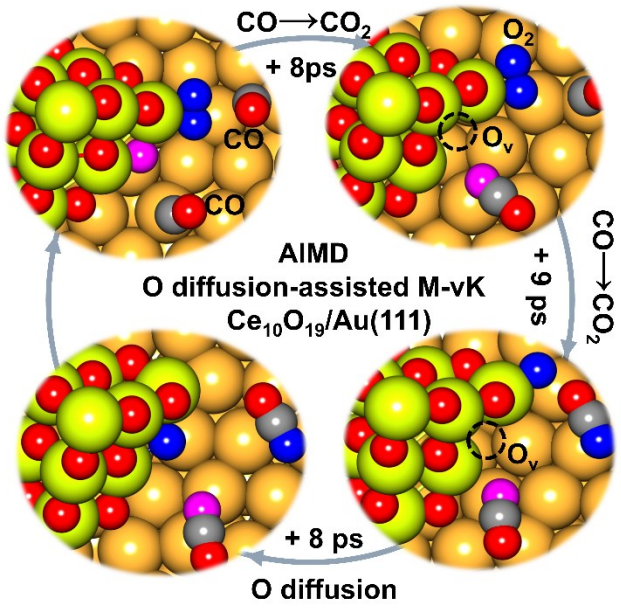

Gold-supported ceria nanoparticles (CeO_x/Au), an inverse system with respect to more common ceria-supported gold nanoparticles, were previously identified as an excellent catalyst for water-gas shift reaction, CO and NO oxidation, and steam reforming of methanol. However, electronic structure and reactivity of such inverse catalysts has not been well understood. To probe the inherent nanoparticle-support interactions and the mechanism of catalytic CO oxidation, *ab initio* molecular dynamics (AIMD) simulations and static DFT computations have been carried out on Au(111)-supported ceria clusters ($Ce_{10}O_{20/19}$), a prototype model system of an inverse CeO_x/Au catalyst. We have identified the perimeter of the supported ceria nanoparticle as the most favorable O vacancy formation site; however, the O vacancy further migrates to an inner interface site during the thermalization process, simultaneously triggering electron transfer from ceria to Au. Our study shows that the Au(111) surface always withdraws electron density from ceria, irrespective of the chemical environment, namely, reducing ($Ce_{10}O_{19}$), neutral ($Ce_{10}O_{20}$), or oxidizing (presence of surface O) environment. To mimic the realistic catalytic environment, CO and O_2 were at the same time pre-adsorbed on the surface of the composite catalyst. We find a vacancy diffusion-assisted Mars-van-Krevelen type of reaction mechanism, in which the first CO molecule reacts with the lattice O atom of ceria rather than with the activated O_2^{2-} species forming CO_2 and leaving one O vacancy behind. This vacancy becomes subsequently refilled by the O atom diffused from the site of O_2 reaction with the second CO molecule, recovering the complete framework of the $Ce_{10}O_{19}$ and closing the catalytic cycle. Finally, we discuss the differences and similarities between ceria/Au and Au_n/ceria with respect to such chemical and physical phenomena as the surface dynamics, charge transfer between the gold and the oxide phases, and the mechanism of CO oxidation.

Introduction

Ligand-functionalized and oxide-supported gold nanoparticles have been intensively studied in catalytic science over the past three decades, and considerable progress has been achieved in understanding the underlying catalytic mechanisms.[1-7] In contrast, the mechanistic understanding of catalytic processes ocurring on nanoporous gold (np-Au), a three-dimensional nanoporous material, is still far less developed, even though high activities and selectivities have been observed in (partial) oxidation reactions.[8-12] Theoretical studies have been debating on the mechanism of such reactions with dioxygen on np-Au, especially on the role of under-coordinated surface atoms and impurities of a less noble metal (usually silver) left over from the preparation of npAu, which is obtained by selective leaching this less noble metal out of a corresponding Au alloy.[13-18] Whereas most studies suggest a significant participation of the second metal (Ag) in the activation of O_2 on the surface of npAu, some studies also suggest a possible role of chemisorbed oxygen on Au sites in facilitating O_2 dissociation,[17, 19] or as a driving force for Ag segregation to the surface.[13, 20] The remarkable catalytic activity and high selectivity of nanoporous gold render this material interesting for a variety of practically interesting reactions ranging from CO oxidation to more complex organic transformations.[21-24] However, an possible limitation when envisioning a use of npAu in commercial catalysis is the limited thermodynamic stability resulting from the nanosize of its ligaments in the range of a few 10 nm and its therefore high surface energy. In particular, adsorbed species may trigger surface diffusion and restructuring, thus leading to coarsening of its nanoporous structure.[9, 19, 25-28] In other case, the dioxygen atomsphere can increase the stablity of np-Au.[29] Our recent theoretical studies[13, 19, 30] predicted adsorbate-induced surface restructuring through –(O–Au)– chain formation on np-Au after the adsorption of O atoms. Importantly, formation of similar oxygen chain structures was computationally predicted to be favorable on the Au(111),[31] Au(110),[32,33] and AgAu(211)[17] surfaces. The oxygen-driven surface evolution and the enhancing role for a Ag segregation to the surface of ligaments in nanoporous gold have been revealed in our previous study based on *Ab Initio* Molecular Dynamics simulations (AIMD).[13]

To reduce thermal and possible reaction-induced coarsening of npAu, deposition of nano-sized oxide particles (TiO_2 or CeO_2) has been proven to be an opportunity to drastically improve the thermal stability of the material and at the same time to increase its catalytic activity.[25, 34-37]

The TiO_2 and CeO_2 nano-particles supported on Au(111) and on np-Au have been found to be effective catalysts for the CO oxidation and NO reduction,[34, 36, 38-39] water-gas shift reaction[34, 36, 40-42] and steam reforming of methanol.[43]

To the best of our knowledge, theoretical studies on gold catalysts functionlized with nano-metallic-oxides (the inverse systems with respect to oxide-supported Au nanoparticles) are rare (in fact, we are aware of only one work[44] that dealt with O vacancy formation for such ceria/gold system) so that mechanistic details of oxidation reactions on such inverse catalysts still remain unclear. For the oxide supported Au nanoparticle catalysts, it is generally recognized that the Au–oxide interfacial perimeter plays an important role.[45-50] The reactivity of such two-component catalysts is affected by the structural and electronic properties of Au particles, the interaction between the support and Au particles, and adsorbates. As a well-studied example, ceria (CeO_2) has been found to be an effective support for nanoparticulate gold catalysts; the high catalytic activity has been attributed to the easy formation of oxygen defects, the high oxygen storage capacity of ceria, and the facile acceptance/release of excess electrons.[51-52] Various studies have identified interface sites between the ceria support and the deposited gold particles to play vital role for adsorpiton and activation in the catalytic reactions.[53-56] As for the dynamics of such catalyst, the environmental transmission electron microscopy analyses[6] revealed that gold nanoparticles on CeO_2 support change their shapes at the interfacial area in response to alternating oxidizing and reducing atmospheres.

The TiO_2 and CeO_2 supported Au nano-particles have been widely and well studied with respect to many aspects including catalytic properties and pertinent mechanistic details, chemistry and physics of the interface, charge transfer.[44, 47, 57-62] In addition to experimental studies, also theoretical studies have been carried out mainly at the density functional theory (DFT) level, revealing electronic structures, interfacial dynamics during catalytic processes, even predicting the dynamics of Au single-atom catalysis mechanism on ceria.[47, 57] Whereas bulk gold is notoriously inert, reducible-oxide particles supported on Au surfaces demonstrated remarkable catalytic activity and high selectivity, as mentioned above. It has been suggested that oxygen vacancies (denoted O_V hereafter) in the oxide nanoparticles probably play a key role for the enhanced activity observed for such catalysts.[41] Among other oxides (such as titania and also binary oxides) cerium

oxide has been used to functionalize nanoporous gold and a high concentration of O vacancies was inferred from studying the Ce^{3+}/Ce^{4+} ratio with XPS for prepared catalyst.[41-43] Another aspect relevant for such inverse Au catalyst systems are electron transfer processes which are expected to be different from oxide-deposited Au nanoparticles, since npAu exhibits a (bicontinous) porous network so that it represents a conducting support. One can thus anticipate that gold-supported oxide nanoparticles and oxide-supported gold catalysts might show different physical-chemical behavior, interfacial dynamics, electronic structure and catalytic mechanisms in surface reactions.

In view of these fundamental questions, understanding the restructuring and dynamic evolution of oxide nanostructures on gold surfaces becomes very intriguing and important for elucidating the catalytic behavior of functionalized np-Au at the atomic scale. In this work, we use theoretical models to reveal the structural and dynamic properties of Au supported CeO_2 nanoparticle and to investigate the reaction mechanism and dynamics of oxidative catalysis on such nanoparticles. In our models, a pyramidal $Ce_{10}O_{20}$ cluster will be used to represent a ceria nanoparticle. This nanoparticle is deposited on a flat Au(111) surface representing the model system studied here will be used to represent the Au support because this simple surface can already reflect the chemical nature of extended Au surfaces and can mimics the flat part of np-Au ligaments, where (111) facets are dominant.[8] Neither the low-coordinated Au atoms (also abundant on np-Au) nor impurities of a less noble metal (present in small amounts) are captured by this simplified model; nevertheless, we argue that such a model is a reasonable starting approximation, capturing the essential elements of the interaction of a massive Au body with a finite oxide nanoparticle. The objectives of the present work are to determine the most favorable oxygen vacancy formation sites at the supported CeO_2 nanoparticles, to characterize the structural rearrangements and dynamics in the surface region associated with the dioxygen activation and CO oxidation reaction. Furthermore, the electronic structure of CeO_2/Au(111) system and defect chemistry and physics during catalytic CO oxidation will be explored as well. Ab initio molecular dynamics (AIMD) simulations have been carried out to provide deeper insight into such "inverse catalyst" CeO_2/Au(111) model system.

Computational Details

In this work, we applied a combination of ab initio molecular dynamics (AIMD) simulations and

standard (static) DFT computations to study surface and interface evolution and chemical reaction (CO oxidation) on the gold-ceria bifunctional catalyst. The AIMD simulations allow us to explore time-evolution of complex condensed-phase systems at a given temperature and to find low-energy reaction pathways. The static DFT-based approach was used to compute activation barriers, which are not directly available from AIMD.

We employed a *p*(5×5) unit cell of the regular Au(111) surface with a slab thickness of 5 atomic layers and ~24 Å vacuum space separating the slab from its periodic image in the Z direction. The bottom 2 layers of the slab were frozen while the top 3 layers were allowed to relax without constraints. Ceria clusters of various size and shape have been investigated and compared. We have chosen tetrahedral $Ce_{10}O_{20}$ as one of the stable ceria clusters of intermediate size for our model[63-64] in combination with the Au(111) slab to construct the prototypical gold-supported oxide model system. The AIMD simulations were performed using the CP2K package.[65] All initial geometries that served as input for AIMD simulations were fully optimized to a local minimum by means of electronic and geometric structure relaxations performed with CP2K. The computed electronic properties of ceria are very sensitive to the Hubbard U-J value. We adopt the U-J value of ~7 eV that was previously found to successfully predict the chemical and electronic properties of CeO_2.[47] The generalized-gradient approximation in the parameterization of Perdew, Burke, and Ernzerhof (PBE)[66-67] was used to compute the exchange-correlation energy. The choice of the PBE functional is justified by its very good performance in describing bulk properties of transition metals.[68-69] In view of various interacting adsorbates on the Au(111) surface, the long-range interaction is none-negligible, thereby, dispersion interaction was considered in all calculations by using empirical parameterized Grimme (D3) method.[70] The valence electrons ($5d^{10}6s^1$ for Au, $4f^15s^25p^65d^16s^2$ for Ce, $2s^22p^4$ for O and $2s^22p^2$ for C) were described using hybrid Gaussian and plane-wave (GPW) basis sets,[71] and the cutoff energy of 500 Rydberg for auxiliary plane-wave basis sets was adopted in all computations. We employed special double-ζ valence plus polarization (DZVP) basis sets optimized to minimize basis set superposition errors.[72] Core electrons were described with scalar relativistic norm-conserving pseudopotentials.[73] Brillouin zone integration was performed with a reciprocal space mesh consisting of only the gamma point. In the simulations, we used the Nose-Hoover thermostat (NVT) to sample from the canonical

ensemble.[74-75] The relatively short time scales of AIMD (time step of 0.5 fs and a total time of a simulation run of up to 30 ps) limit the sampling to only fast low-energy-barrier events. To rapidly explore a large phase space volume of surface configurations, statistical sampling was performed at an elevated temperature of 700 K. This strategy was previously successfully employed in a number of AIMD studies.[57, 76] The structures were relaxed until the force acting on each atom was $\leq 2\times10^{-2}$ eV $Å^{-1}$. Transition states were predicted using the climbing image nudged-elastic-band method (CI-NEB) with a convergence criterion of 0.05 eV/Å.[77]

Results and discussion

Structural dynamics and electronic structure of Au(111) supported ceria nanoparticles

The bulk gold is chemically inert, whereas the ceria nanostructures supported on Au(111) or on np-Au exhibit remarkable catalytic activity, as discussed in the introduction. Therefore, one can expect that ceria nanoparticles play an important role in generating catalytically active sites in the CeO_2/Au(111) catalytic system. Specifically, in ceria-functionalized np-Au, the oxide component not only enhances the activity, but also directly contributes to the stability of the np-Au skeletal framework.[41-42] Therefore, understanding the structural dynamics, interfacial chemical-physical interaction, vacancies formation, and electron transfer between the gold support and ceria nanoparticles is essential for gaining a deeper insight into catalytic properties of such an inverse catalyst. In this study, our realistic chemical model of Au(111)-supported ceria cluster ($Ce_{10}O_{20}$ or a reduced counterpart with one O vacancy, $Ce_{10}O_{19}$) was computationally characterized, and the structural dynamic evolution, formation of oxygen vacancies, and changes in electronic structure have been investigated by using AIMD simulations and DFT static computations. Selected trajectories (from 0 ps to 24 ps) of the simulated structural evolution of $Ce_{10}O_{20}$/Au(111) at 700 K are shown in **Fig**. **S1**. The supported stoichiometric ceria nanocluster keeps its pyramidal shape on the Au(111) surface during the thermodynamically driven evolution, revealing that the nanoparticle is rigid and stable, which is consistent with TEM experimental observations.[41] In this respect, it is interesting to make a comparison to supported Au nanoparticles, for which experimental and theoretical studies demonstrated that the Au nanoparticles are “melting” and

wetting ceria support.[47] The dynamic structure of Au-supported ceria nanoparticle is found to be very different. In this work, the binding energy of $Ce_{10}O_{20}$ on Au(111) was computed at -2.28 eV. The ceria nanoparticles supported on np-Au have been found to be rich in O_V defects;[41] therefore, exploring the defect chemistry of our supported ceria nanocluster can provide important insights for understanding mechanism of catalytic reactions. Herein, we investigated the formation of O_V defect sites at the ceria-gold interface and at various locations on the $Ce_{10}O_{20}$ cluster, as shown in **Fig**. **1a**. In a real catalytic system, oxygen vacancies are probably arise through deoxygenation, or reduction reaction, such as $CO + O \rightarrow CO_2$. For convenient discussion, the calculated vacancy formation energies are referred to one half of the total energy of O_2 molecule (instead of O atom) plus the energy of the defected $Ce_{10}O_{19}$/Au(111) system, as it has been widely adopted in previous theoretical studies. The vacancy formation energies $E(O_V)$ are calculated as follows

$$E(O_V) = E(Ce_{10}O_{20}/Au111) - 1/2E(O_2) - E(Ce_{10}O_{19}/Au111)$$

where the $E(Ce_{10}O_{20}/Au111)$, and $E(Ce_{10}O_{19}/Au111)$ are the DFT total energies of the none-defective, and reduced models, respectively, and $E(O_2)$ is the energy of the gas-phase O_2. There are four different types of O vacancies determined by the symmetry of the $Ce_{10}O_{20}$ cluster and the inequality of once facet due to its interaction with the Au(111) surface. The O_V formation energies at different sites shown in **Fig**. **1a** and designated as **I**, **II**, **III, IV** are 1.71, 2.13, 1.81, and 3.13 eV, respectively. The most energetically preferred O_V defect formation site (**I**) with the lowest $E(O_V)$ is located at the interface (edge site of the $Ce_{10}O_{20}$ cluster) between the $Ce_{10}O_{20}$ cluster and the Au(111) surface. Hence, our results suggest that the interfacial perimeter between ceria and Au support should be the most probable place for O_V formation in Au-supported ceria catalysts at current situation. The formation of two oxygen vacancies was considered as well, and the computed formation energy of the second O_V at the perimeter was found larger than 4.5 eV, which suggests that spontaneous formation of more than one defect per this particle size (by simple loss of O) should be an event of low probability. In our theoretical chemical model, $Ce_{10}O_{19}$/Au(111) with one O vacancy, two resulting Ce^{3+} centers generate a ratio of 20% Ce^{3+} that is close to the experimental XPS result.[41] Assuming a perfect Au-supported ceria particle without defects, removal of O atoms through deoxygenation reactions will most likely create O_V at the interfacial site (**I**). Alternatively, a vacancy could also be generated at other sites (**II**/**III**/**IV**-O_V), e.g. if CO

react on top of the ceria particle and not at the gold-ceria interface. Eventually, the vacancy migrates to site **I** releasing energy during thermalization and equilibration process. The computed spin density of **I**-O_V with the spin population value of 1.84 μ_B is shown in **Fig**. **1c**. The spin density implies that the O_V formation will leave two electrons to localize on two Ce sites forming Ce-$4f^2$ (Ce^{3+}) electronic configuration. We have also computed the low-spin state of the **I**-O_V structure with two 4f electrons delocalized at the interface, the low-spin state lying higher in energy than the localized spin state by 0.98 eV.

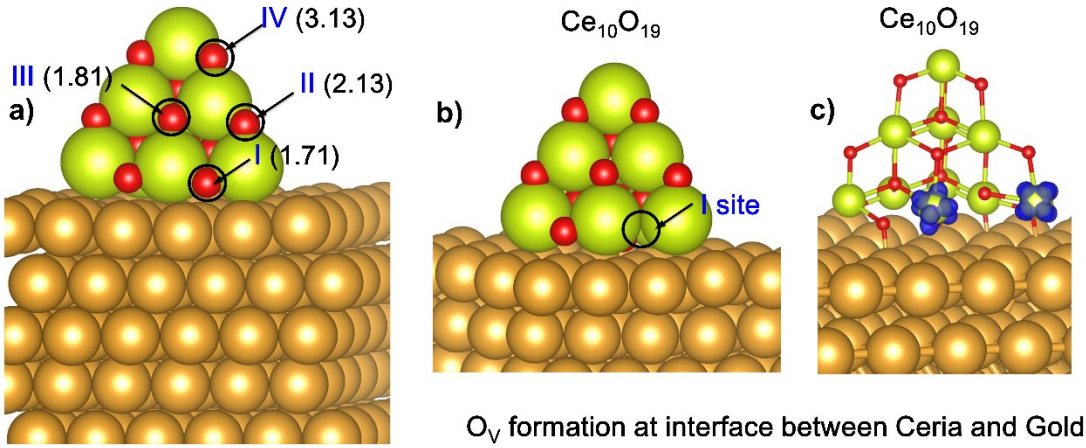

Fig. 1 a). Computed O_V formation energy $E(O_V)$ (in eV) at different sites of $Ce_{10}O_{20}$. The most energetically favorable site (**I**) is located at the interface between $Ce_{10}O_{20}$ and Au(111). **b)** Geometry of the $Ce_{10}O_{19}$ cluster with one O vacancy, **c)** Distribution of the spin density with a spin population of 1.84 μ_B on two adjacent Ce atoms.

As mentioned above, we found that the $Ce_{10}O_{20}$ cluster on the gold surface is thermodynamically stable as follows from the AIMD simulation during 24 ps at 700 K. Next, we studied the structural dynamics and stability of the Au-supported reduced $Ce_{10}O_{19}$ nanoparticle with the O_V defect at the most favorable position **I** (at the gold ceria perimeter), which should help us in understanding its catalytic properties. From the AIMD simulation, we found that O_V migrates from the perimeter site **I** to the inner bottom site **V** of the $Ce_{10}O_{19}$ nanoparticle after 1.2 ps of thermodynamic evolution, as shown in **Fig. 2**. The computed vacancy formation energy is 0.97 eV for site **V**. For comparison, $E(O_V)$ = 1.73 eV in free $Ce_{10}O_{20}$ for O removal at the same site; hence,

interaction with the support reduces the O vacancy formation energy. Meanwhile, the spin density vanishes (the spin population value changing from 1.84 to 0 μ_B) once O_V migration has been completed (**Fig. 2**), implying an electron transfer promoted by the O_V migration. In order to confirm the electron transfer and to reveal the fate of the two 4f electrons initially localized on two Ce^{3+} centers (transfer to interior Au or delocalization on the interface or within the cluster), a charge density difference analysis was carried out, as shown in **Fig. 3a**. The increase in charge density at the gold-ceria interface indicates that the two 4f electrons become delocalized at the interface between the Au(111) surface and ceria cluster ($Ce_{10}O_{19}$) after the oxygen vacancy migration. A Bader charge population analysis shows that the $Ce_{10}O_{19}$ cluster transfers 1.52 e to surface Au; the average charge obtained on interfacial Au atoms is 0.16 e. For a stoichiometric $Ce_{10}O_{20}$ cluster on Au(111), the charge polarization also exists and is shown in **Fig. 3b**, which also implies a strong interaction between the gold support and ceria cluster. The charge transfer from $Ce_{10}O_{20}$ to surface Au is 0.50 e; each interfacial Au atom gains negative charge of 0.13 e, as derived from Bader charge population analysis. Our study shows that in the inverse CeO_x/Au catalyst the charge transfer direction between gold and ceria is different from the Au_n/ceria system, in which charge transfer direction depends on the redox atmosphere.[47] The charge accumulation at the interface can provide excess electrons to facilitate the adsorption and activation of the O_2 molecule in aerobic oxidation reactions. The structural dynamics and evolution of the Au-supported $Ce_{10}O_{19}$ cluster with an oxygen vacancy located at the inner position **V** at the gold-ceria interface was further evaluated via an AIMD simulation. From a snapshot of the AIMD simulation shown in **Fig**. **S2**, we find that the reduced cluster with oxygen vacancy of type **V** is very stable. The ceria particle is found to be rigid, as it maintains its original shape during the simulation. That is different from the surface wetting by Au nanoparticles in the Au_n/ceria system facilitated by charge transfer.[6, 47] It is interesting to investigate whether the vacancy migration is reversible, i.e. whether O atoms on the Au surface would spontaneously fill the vacancy. Therefore, we placed two O atoms near two bottom corner Ce atoms and carried out an AIMD simulation at 700 K for 24 ps (**Fig**. **S3)**. No O atom diffusion to the inner O vacancy of type **V** was observed. By the end of the simulation, the O vacancy was still located at the same position within the cluster. Hence, we conclude that

spontaneous vacancy filling for the vacancy of type **V** should be a low-probability event due to a high barrier for vacancy filling.

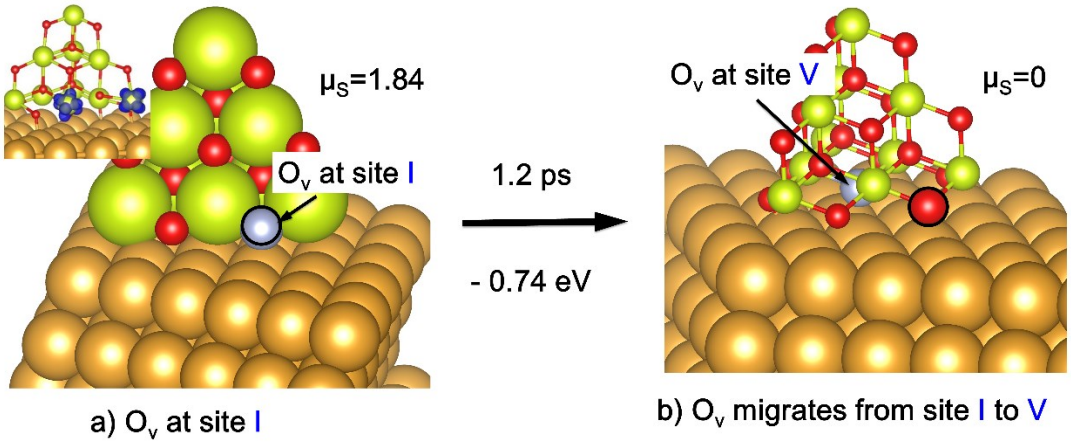

Fig. **2** The thermodynamically driven O_V migration from site **I** to the bottom face-centered site **V** of the $Ce_{10}O_{19}$ nanocluster. **a)** Structure and spin density of Au-supported $Ce_{10}O_{19}$ cluster with O_V at position **I** (shown in gray color). Two unpaired electrons are localized on two Ce atoms forming Ce-$4f^2$ electronic configuration. **b)** System evolution after 1.2 ps AIMD simulation. O_v is transferred to the inner face-centered site **V**, while the magnetic moment changes from 1.84 to 0 μ_B indicating that two unpaired electrons delocalize resulting in the Ce-$4f^0$ electronic configuration.

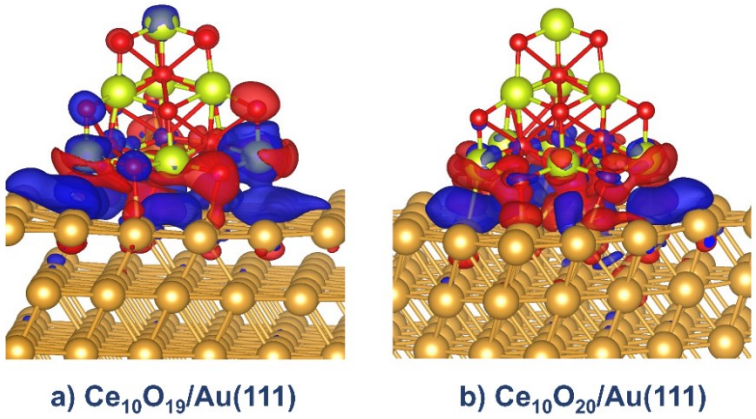

Fig. **3** Charge density difference analysis for Au-supported ceria nanoparticles: a) a reduced $Ce_{10}O_{19}$ particle with a **V**-type vacancy, b) perfect stoichiometric $Ce_{10}O_{20}$ model without a vacancy. The charge density difference was computed according to $\Delta\rho = \rho_{AB} - \rho_A - \rho_B$, where A and B stand for Au(111) and $Ce_{10}O_{19/20}$. Electron density increase is shown in blue, electron density decrease is shown in red (isovalue: 0.01 au).

To gain deeper understanding of the strong interaction between the Au support and the $Ce_{10}O_{19}$ cluster, we have computed a one-dimensional potential energy curve for the adsorption of a defective $Ce_{10}O_{19}$ cluster onto the Au(111) surface. We followed the energy and electronic structure changes along the reaction coordinate (defined with respect to the cluster-surface distance) while the cluster was approaching the surface, as shown in **Fig. 4**. In the initial $Ce_{10}O_{19}$ cluster far from the Au surface O_V was located at the center of a facet, and that facet was directed towards the Au surface as the cluster approached the surface, so that the final geometry corresponded to O_V in the inner position **V** at the CeO_x/Au interface, the lowest-energy configuration discussed above. Initially, the $Ce_{10}O_{19}$ cluster far from the surface had a spin magnetic moment $\mu_s = 2\ \mu_B$ corresponding to two unpaired 4f electrons spreading over three Ce centers at the corners of the defected triangular facet, **Fig. 4**. However, as we found out earlier (**Fig. 2b**), in the final geometry the fully stabilized $Ce_{10}O_{19}$ cluster on gold has Ce-$4f^0$ (Ce^{4+}) configuration. The adsorption energy of the $Ce_{10}O_{19}$ cluster in that adsorption configuration is -3.03 eV. According to Marcus electron-transfer theory, electron transfer occurs when the potential energy surfaces of two different electronic states cross. In order to verify the potential energy surfaces crossing, two energy curves (for the high- and low-spin states) were obtained by varying the distance between the $Ce_{10}O_{19}$ cluster and Au support as shown in **Fig**. **4**. Two potential energy curves corresponding to the two different electronic states, Ce-$4f^2$ (black curve) and Ce-$4f^0$ (red curve), are shown in **Fig. 4**, where the crossing between the two potential energy curves indicates a possibility of an electron transfer (to the Au surface), further implying the oxidation state change from Ce^{3+} to Ce^{4+}. Here, the Ce-$4f^2$ notation refers to the electronic state of the whole system, implying a formal localization of two 4f electrons on Ce atoms. These two 4f electrons are, however, distributed between three Ce atoms according to the calculated spin density (**Fig. 4**).

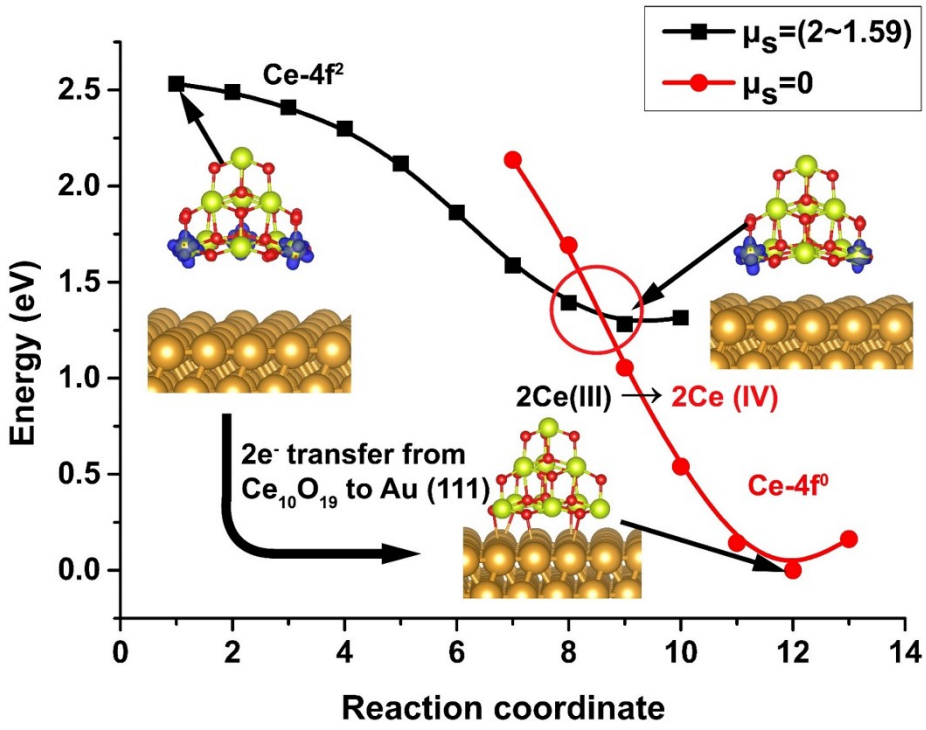

Fig. 4 Potential energy surface scans. Two potential energy curves for the high-spin and low-spin states denoted Ce-4f^2 and Ce-4f^0 were obtained along the reaction coordinate. The reaction coordinate was generated by a linear interpolation between the geometries of the desorbed and adsorbed $Ce_{10}O_{19}$ particle. The values of reaction coordinate correspond to generated images between the initial and final geometries. These curves cross at some point allowing the transfer of two electrons to Au. The spin magnetic moment μ_s changes from ~2 to 0 μ_B in the overall process.

Adsorption and activation of O_2

In a previous study, the oxygen molecule has been found to preferentially adsorb at the O_V site of the ceria-supported gold nanoparticle system to be activated after O vacancy generation from CO oxidation.[47] That study also found that the O_2 molecule adsorption on a perfect ceria surface and the interface is relatively weak.[47] Therefore, it is an interesting and fundamental question, whether or not the dioxygen adsorption and activation on the gold-supported ceria follows the same mechanism as on the ceria-supported gold nanoparticle. Here we calculated the adsorption of O_2 on the defective (O_V in position **V**) and perfect models of gold-supported clusters $Ce_{10}O_{19}$/$Ce_{10}O_{20}$. Possible adsorption sites and geometric configurations of the adsorbed O_2 molecule on Au-

supported ceria clusters have been predicted for both chemical models and are shown in **Figs**. **S4** and **S5**. No O_2 molecule adsorption on Au atoms other than perimeter sites of $Ce_{10}O_{19}$/$Ce_{10}O_{20}$ nanoparticle was found in our studies, consistent with previous reports of very weak or even repulsive interaction between O_2 and Au(111).[78] The adsorption energy of O_2, the O-O bond length, and the net spin population on the O_2 molecule adsorbed at several possible adsorption sites are given in **Fig**. **S4** and **S5**. The most energetically favorable adsorption site is the same for the ($Ce_{10}O_{19}$/Au) and perfect ($Ce_{10}O_{20}$/Au) models. O_2 adsorbs most strongly at the bottom corner sites of the pyramidal ceria cluster, at the interface between the cluster and the Au(111) surface, as shown in **Fig**. **5**. The adsorbed O_2 chemically binds to one unsaturated Ce atom (with the coordination number 4) and two Au atoms. The spin population values on O atoms in the most energetically favorable adsorption geometry of O_2 in both cases ($Ce_{10}O_{19}$ or $Ce_{10}O_{20}$ clusters) are 0, implying a change from a triplet O_2 to a singlet O_2^{2-} and a lengthening of the O-O bond from 1.26 to 1.46 and 1.44 Å, respectively, as illustrated in **Fig**. **5**. The adsorption energies are -0.80 eV and -0.75 eV, respectively. The O_2 adsorption energies on Au_{20} or interfacial sites of ceria supported gold cluster system are predicted to be weaker than -0.2 eV,[47] indicating much weaker adsorption. The O_2 adsorption on the defective $Ce_{10}O_{19}$ model is slightly more energetically favorable than on the perfect model by 0.05 eV. If the O_V is located at the particle perimeter (site **I**), the O_2 adsorption at the vacancy site is even weaker, -0.48 eV. Hence, we propose that the presence of oxygen vacancies in the gold-supported ceria particles is not the decisive factor for the oxygen adsorption and activation. As we discussed in the previous section, the electron density accumulates at the interface between ceria and gold, and that increased electron density region can promote O_2 adsorption and activation. These findings suggest that it is the charge polarization between ceria and gold that facilitates O_2 adsorption and activation. In contrast, we found that O_2 adsorbs only very weakly on the free $Ce_{10}O_{20}$ cluster, while its adsorption energy on $Ce_{10}O_{19}$ is -0.60 eV, as shown in **Fig. S6**. O_2 adsorbs on a vacancy site forming O_2^- species with the O-O bond elongated to 1.34 Å. The dissociation energy of O_2 on $Ce_{10}O_{19}$ is 1.02 eV implying a high activation barrier.

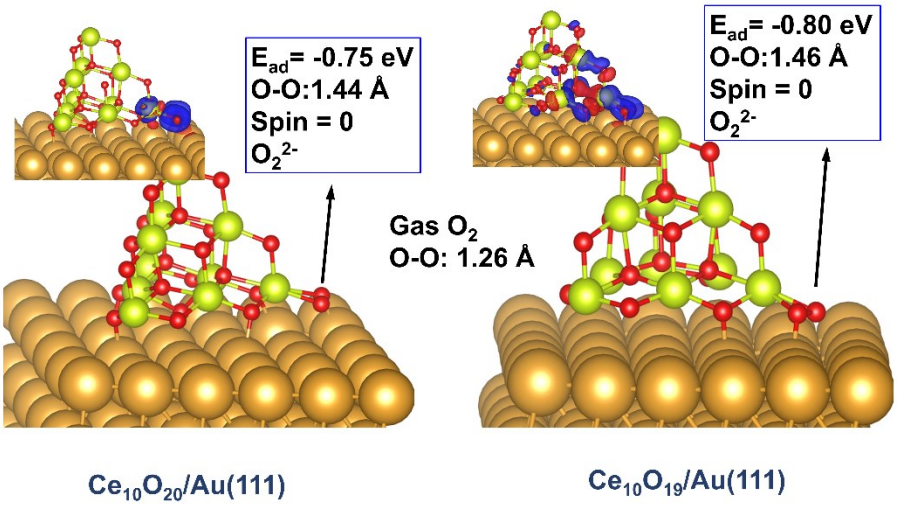

Fig. 5 The most energetically favorable O_2 adsorption sites at the Au-supported $Ce_{10}O_{19}$ and $Ce_{10}O_{20}$ clusters. The corresponding charge density difference for O_2 adsorption and activation are shown as well. The charge density difference was computed according to $\Delta\rho=\rho_{AB} - \rho_A - \rho_B$, where A and B stand for $Ce_{10}O_{19/20}$/Au(111) and O_2. Electron density increase is shown in blue, electron density decrease is shown in red. (Isovalue: 0.02 au.)

CO oxidation mechanism

The mechanisms of catalytic CO oxidation by O_2 on ceria-supported gold nanoparticles have been extensively studied. Three main types of CO oxidation mechanisms have been theoretically proposed:[51, 56, 79] (1) CO oxidation by co-adsorbed O_2 on Au particles, (2) CO oxidation by adsorbed O_2 at the interfacial site and (3) CO oxidation by a lattice oxygen ion from the CeO_2 substrate. Recent studies suggested that CO reaction with pre-adsorbed O_2 on a gold nanoparticle or ceria-gold interface is less probable than the reaction with the lattice O because of the weak adsorption (weaker than -0.2 eV) of O_2 on the gold cluster and at the ceria-gold interface (if ceria is not reduced); instead, they favor Mars-van-Krevelen mechanism (3).[44, 47] The study of ref. 42, in addition, proposed a formation of Au^+-CO species that can detach from Au nanoparticles and react with lattice O or with O_2 adsorbed at a vacancy site. In our current study of CO oxidation on gold-supported ceria clusters, we find that the O_2 molecule strongly binds at the interface in both defective and non-defective systems with significantly weakened O-O bond preparing it for an

easy reduction by a CO molecule. It has been reported that the O_V concentration in gold-supported ceria may vary from 3% to 18% depending on the ceria loading on the gold surface.[40] In our study, we adopted the $Ce_{10}O_{19}$ cluster model with 5% O_V, which is consistent with the experimentally determined range above. In the AIMD simulation to be described below, we have started from an initial state in which CO and O_2 molecules are pre-adsorbed (O_2 adsorbs on the gold-ceria interface and CO adsorbs on Au, as CO adsorption on ceria is too weak, **Fig. S6**). The adsorption energy of CO on the Au surface is -0.80 eV for each CO molecule. We find that in the absence of ceria nanoparticle, the adsorption energy of CO on the Au(111) surface is weaker, about -0.45 eV (**Table S1**). The presence of the $Ce_{10}O_{19}$ cluster on Au(111) increases the magnitude of CO adsorption energy by ~0.12 eV, and the co-adsorption with O_2 further slightly increases it by 0.03 eV. When comparing our calculated CO adsorption energy with experimental and other theoretical values,[80-81] we conclude that the dispersion-corrected PBE-D3 functional likely overestimates it.

In view of the expected presence of oxygen vacancies in gold-supported ceria catalysts, we have chosen the defective $Ce_{10}O_{19}$ model to study CO oxidation mechanism. As discussed in the previous section, the O_2 molecule adsorption on Au-supported $Ce_{10}O_{19}$ releases 0.80 eV energy, which elongates the O-O bond distance from 1.26 to 1.46 Å and transfers two electrons to the O_2 molecule forming O_2^{2-} species. We have placed two O_2 and two CO molecules near the $Ce_{10}O_{19}$ cluster supported on Au(111), so that each O_2 molecule was adsorbed at one of the three vertex sites at the bottom of the ceria cluster of $Ce_{10}O_{19}$ and CO molecules adsorbed upright on top of Au atoms not far from the ceria nanoparticle, as shown in **Fig. 6**. The average adsorption energy of O_2 in this initial structure is -0.78 eV per O_2 molecule. No significant difference in geometry or spin population was found in comparison to the adsorption of only one O_2 discussed above. Starting from this initial structure, an AIMD simulation (**Fig. 6**) was carried out to explore the catalytic reaction of CO and O_2 at 700 K chosen as simulation temperature. The first CO molecule was oxidized into CO_2 by the lattice O atom of the $Ce_{10}O_{19}$ nanocluster rather than by the adsorbed O_2 molecule after 7 ps simulation, leaving an oxygen vacancy behind. The second CO molecule was oxidized by the adsorbed O_2 molecule after further 10 ps of simulation as shown in **Fig. 6**, generating atomic O bound to Ce. The atomic O then diffused and filled the oxygen vacancy generated from the first CO oxidation by lattice O.

Surprisingly, the first CO molecule reacts with the lattice O atom rather than with the activated O_2^{2-} species, while the second CO molecule reacts with the O_2^{2-} species to form CO_2 molecule and an O atom coordinated with the corner Ce atom. Therefore, one oxygen vacancy and one extra O atom remain on the ceria particle after the oxidation of two CO molecules. Finally, the O atom migrates to the oxygen vacancy site to recover the complete framework of $Ce_{10}O_{19}$. The accurate reaction energy profile including reactants, transition states, intermediates, and products of all elementary steps revealed during AIMD simulation was subsequently refined using static calculations and is shown in **Fig. 7**.

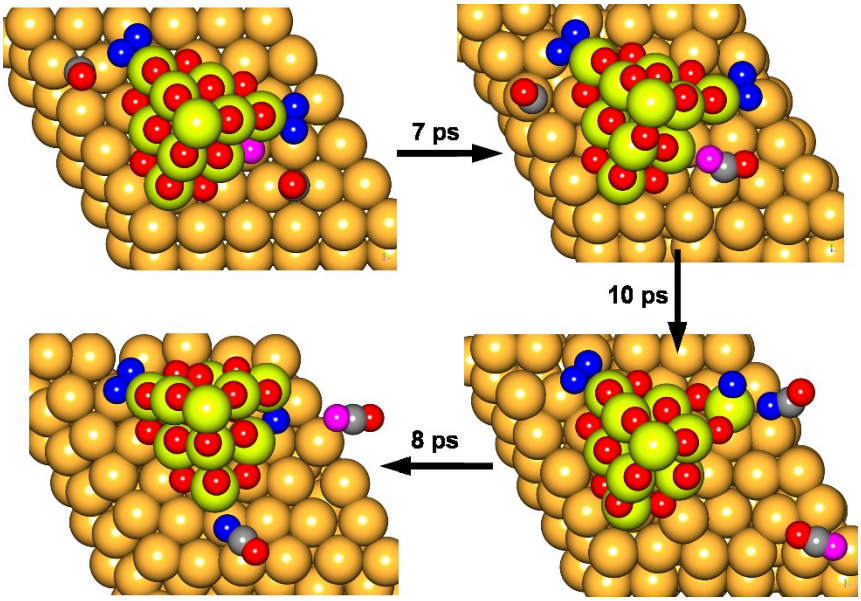

Fig. **6** The AIMD simulation of CO oxidation reaction on Au-supported $Ce_{10}O_{19}$. Color coding of elements: orange, Au; lime, Ce; red and magenta, O; blue, adsorbed O_2; gray, C.

In the first step of the reaction path **I-ts1-II,** shown in **Fig**. **7**, the first CO molecule reacts with the lattice O atom of ceria nanoparticle located at the edge perimeter site to form a CO_2 molecule with the activation energy of only 0.21 eV and the reaction energy of -1.16 eV. Meanwhile, the energy barrier for the CO reaction with the adsorbed O_2 is computed as 0.34 eV, implying that it is kinetically less preferable in comparison to the CO reacting with the O atom of the ceria nanoparticle. The generated CO_2 adsorbs in a monodentate fashion with O atom coordinated to the basal Ce atom at the O vacancy with a slightly bent O-C-O angle. It can desorb with the desorption energy of 0.52 eV through the **II-III** reaction path. The second CO is oxidized

by the activated O_2^{2-} species forming CO_2 and an O atom coordinated to a corner Ce atom in the **III-ts2-IV** reaction path, for which the activation barrier and reaction energy were computed at 0.30 eV and -3.04 eV, respectively. The formed CO_2 molecule can directly desorb into the gas phase; the adsorption energy of CO_2 on Au is expected to be very weak. As revealed by the AIMD simulation, the remaining O ad-atom attached to the corner Ce atom, left behind as a result of CO oxidation is thermodynamically unstable, and thus prefers to migrate to the O_V site, as shown in the **IV-ts3-V** reaction path with the predicted migration barrier and reaction energy of 0.20 eV and -1.25 eV, respectively.

For comparison, we have also studied the CO oxidation on the Au-supported $Ce_{10}O_{20}$ particle, although such perfect ceria particles with no vacancies probably do not exist in real catalytic systems. The reaction path is shown in Fig. **S7**, in which the first CO oxidation has the activation barrier of only 0.12 eV; that is even lower than for the CO oxidation on the Au-supported $Ce_{10}O_{19}$ system. This is not unexpected, because the perfect Au-supported $Ce_{10}O_{20}$ particle has a stronger oxidizing ability than the $Ce_{10}O_{19}$ particle due to the higher oxidation state of Ce in the former. After the first CO oxidation, the $Ce_{10}O_{20}$ cluster becomes $Ce_{10}O_{19}$ with one O vacancy of type **I**. The calculated activation barrier for the following CO + O_2 reaction, 0.41 eV, is slightly higher than that calculated above for the $Ce_{10}O_{18}$/Au(111) nanoparticle with two O vacancies. The reaction pathway of Fig. **S7** does not derive from an AIMD simulation but is based on static DFT computations. We expect that, most likely, after the first CO oxidation, the O vacancy in position **I** should migrate to the basal plane of the ceria cluster in position **V** (**Fig**. **S8**) due to the significantly lower energy of that isomer, by 0.6-0.8 eV, depending on the positions of adsorbed O_2 and CO. From that point on, further oxidation will follow the same path as discussed above for the $Ce_{10}O_{19}$/Au system.

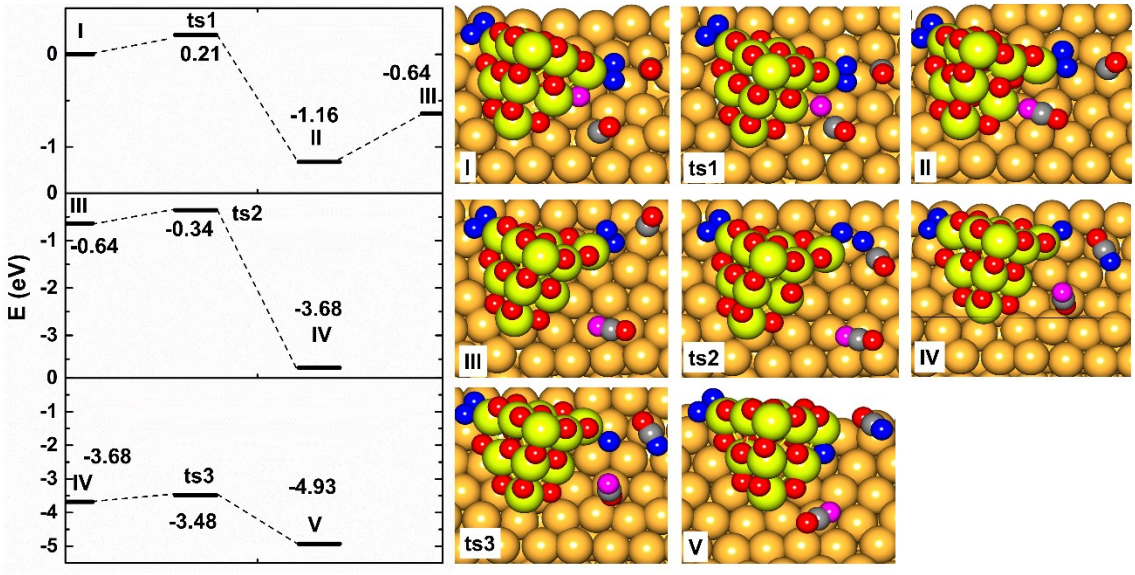

Fig. **7**. Theoretically predicted CO oxidation mechanism catalyzed by the Au-supported $Ce_{10}O_{19}$ cluster. Left panel gives the energy profile of the reaction path. Right panel shows geometries of the reactants, intermediates, transition states and products. The whole reaction mechanism includes three main steps as follows: **I-ts1-II-III** (*CO + $O_{lattice}$→*CO_2, *CO_2→CO_2), the first CO oxidation by an O atom of ceria nanoparticle and the CO_2 desorption; **III-ts2-IV** (*CO + O_2→*O +*CO_2), the second CO oxidation by activated O_2[2]; **IV-ts3-V (***O→$O_{lattice}$**)**, O atom migration to fill the O vacancy. Asterisk symbol indicates adsorbed species. Color coding of elements: orange, Au; lime, Ce; red and magenta, O; blue, adsorbed O_2; gray, C.

Conclusions

In this work, we carried out AIMD simulations and static DFT computations to study the redox chemistry of a gold-supported ceria nanoparticle with the help of the CeO_x/Au(111) computational model. We found that the defective (with one inner O vacancy at the gold ceria interface) as well as stoichiometric Au-supported ceria nanoparticles are thermodynamically stable, as inferred from AIMD simulations at 700 K for 24 ps. For the perfect stoichiometric Au-supported $Ce_{10}O_{20}$ nanoparticle, the most favorable position for O_V formation is the bottom interfacial face centered position, which is, however, buried inside the ceria/Au interface, and presumably O_V at such position cannot be formed directly as a result of deoxygenation. On the surface of the ceria

nanoparticle, the bottom interfacial O at the particle edge is the most favorable site for O_V formation. The O_V formation at that site generates two Ce^{3+} atoms with two localized $4f^1$ unpaired electrons, which prefer to localize on ceria rather than transfer to gold. Nevertheless, the vacancy at this interfacial position is predicted to migrate to a more thermodynamically stable inner interfacial site. This rearrangement is accompanied by a delocalization of two unpaired $4f^1$ electrons on the interface, mainly on interfacial Au atoms. The overall ceria-to-Au charge transfer is suggested to be responsible for the strong particle-support interaction. In contrast, in the Au_n/CeO_2 system the direction of charge transfer depends on the presence of O vacancies in the ceria support, where neutral or positively charged Au nanoparticles were predicted on fully oxidized ceria, while in the presence of Ce^{3+} cations Au acquires partial negative charge.[47, 82-84] The charge transfer facilitates plasticization of the Au nanoparticles in the Au_n/CeO_2 catalyst, whereas the cerium oxide particle always keeps its rigidity on the Au surface, irrespective of the charge transfer.

We found that the charge polarization between the Au(111) surface and ceria increases the electron density at the interface providing electron-rich sites for O_2 adsorption accompanied by O_2 reduction to O_2^{2-}. The preferable adsorption site of the O_2 molecule is at the bottom corner Ce atom at the interface between ceria and the gold surface; the adsorption energies of O_2 are similar on reduced and saturated ceria cluster models. The CO molecule barely adsorbs on a ceria nanoparticle; thus, we did not observe the adsorbate induced supported nanoparticle plasticization. Neither did we find single atom active sites that have been theoretically predicted for the Au/ceria system. [47]

Same as suggested for ceria supported Au nanoparticles, we find the interface between Au and ceria to play a crucial role as active sites for CO oxidation supplying active oxygen atoms from the ceria lattice and providing adsorption sites for O_2 adsorbates. Similar to the findings of Kim and Henkelman for Au_n/CeO_2,[44, 56] in the inverse system CO oxidation also proceeds according to Mars-van-Krevelen mechanism, where CO oxidation with lattice O and the O_2 reaction with CO occur at different active sites and generated O atoms fill up the formed O vacancies. Notably, the O vancancy and atom migration play important roles in recovering the complete framework of the $Ce_{10}O_{19}$ and closing the catalytic cycle.

Although the Au(111) surface orientation is predominant in nanoporous gold and our ceria/Au(111) model provides a first informative insight, one should bear in mind that this is an idealized model. The possible important role of high-index surface orientations, steps and kinks with low-coordinate atoms, presence of Ag impurities and chemisorbed oxygen in the sponge-like nanoporous gold material have not been considered and explored in this work. Further theoretical studies are underway, including these possibly important elements of the Au support material in combination with the supported ceria particles, which will offer deeper insight into the catalytic function of oxide-functionalized nanoporous gold.

Acknowledgments

LVM acknowledges the financial support from the German Research Foundation (DFG) Project No. MO 1863/3-1. We thank the North-German Supercomputing Alliance (HLRN) for providing computational resources.

Supporting Information

Snapshots from AIMD simulations of $Ce_{10}O_{20/19}$/Au(111) supported nanoparticles. Snapshots from AIMD simulation of $Ce_{10}O_{19}$/Au(111) with V-type oxygen vacancy with two added O atoms on the Au support. Structures and energies for O_2 adsorption on Au-supported $Ce_{10}O_{19/20}$. The O_2 and CO adsorption on ceria nanoparticles in the gas phase. The reaction path of CO oxidation on Au-supported $Ce_{10}O_{20}$ particle. CO adsorption energy on the Au(111) surface with different co-adsorbates. Movies illustrating the full catalyzed CO oxidation cycle from AIMD simulations.

References

1. Mikami, Y.; Dhakshinamoorthy, A.; Alvaro, M.; Garcia, H., Catalytic activity of unsupported gold nanoparticles. *Catal. Sci. Technol.* **2013,** *3* (1), 58-69.

2. Hvolbæk, B.; Janssens, T. V. W.; Clausen, B. S.; Falsig, H.; Christensen, C. H.; Nørskov, J. K., Catalytic activity of Au nanoparticles. *Nano Today* **2007,** *2* (4), 14-18.

3. Haruta, M., Gold as a novel catalyst in the 21st century: Preparation, working mechanism and applications. *Gold Bull* **2004,** *37* (1-2), 27-36.

4. Corma, A.; Garcia, H., Supported gold nanoparticles as catalysts for organic reactions. *Chem. Soc. Rev.* **2008,** *37* (9), 2096-2126.

5. Ansar, S. M.; Kitchens, C. L., Impact of Gold Nanoparticle Stabilizing Ligands on the Colloidal Catalytic Reduction of 4-Nitrophenol. *ACS. Catal.* **2016,** *6* (8), 5553-5560.

6. Ta, N.; Liu, J.; Chenna, S.; Crozier, P. A.; Li, Y.; Chen, A.; Shen, W., Stabilized Gold Nanoparticles on Ceria Nanorods by Strong Interfacial Anchoring. *J. Am. Chem. Soc.* **2012,** *134* (51), 20585-20588.

7. Scirè, S.; Liotta, L. F., Supported gold catalysts for the total oxidation of volatile organic compounds. *Appl. Catal. B-Environ.* **2012,** *125*, 222-246.

8. Fujita, T.; Guan, P.; McKenna, K.; Lang, X.; Hirata, A.; Zhang, L.; Tokunaga, T.; Arai, S.; Yamamoto, Y.; Tanaka, N., Atomic origins of the high catalytic activity of nanoporous gold. *Nat. Mater.* **2012,** *11* (9), 775-780.

9. Moskaleva, L. V.; Röhe, S.; Wittstock, A.; Zielasek, V.; Klüner, T.; Neyman, K. M.; Bäumer, M., Silver residues as a possible key to a remarkable oxidative catalytic activity of nanoporous gold. *Phys. Chem. Chem. Phys.* **2011,** *13* (10), 4529-4539.

10. Wittstock, A.; Biener, J.; Erlebacher, J.; Bäumer, M., *Nanoporous gold: from an ancient technology to a high-tech material*. Royal Society of Chemistry: 2012.

11. Lackmann, A.; Mahr, C.; Rosenauer, A.; Bäumer, M.; Wittstock, A., Aerobic Methanol Oxidation over Unsupported Nanoporous Gold: The Influence of an Added Base. *Catalysts* **2019,** *9* (5), 416.

12. Wichmann, A.; Bäumer, M.; Wittstock, A., Oxidative Coupling of Alcohols and Amines over Bimetallic Unsupported Nanoporous Gold: Tailored Activity through Mechanistic Predictability. *ChemCatChem.* **2015,** *7* (1), 70-74.

13. Li, Y.; Dononelli, W.; Moreira, R.; Risse, T.; Bäumer, M.; Klüner, T.; Moskaleva, L. V., Oxygen-Driven Surface Evolution of Nanoporous Gold: Insights from Ab Initio Molecular Dynamics and Auger Electron Spectroscopy. *J. Phys. Chem. C* **2018,** *122* (10), 5349-5357.

14. Dononelli, W.; Tomaschun, G.; Klüner, T.; Moskaleva, L. V., Understanding Oxygen Activation on Nanoporous Gold. *ACS. Catal.* **2019,** *9* (6), 5204-5216.

15. Xu, C.; Su, J.; Xu, X.; Liu, P.; Zhao, H.; Tian, F.; Ding, Y., Low Temperature CO Oxidation over Unsupported Nanoporous Gold. *J. Am. Chem. Soc.* **2007,** *129* (1), 42-43.

16. Fajín, J. L. C.; Cordeiro, M. N. D. S.; Gomes, J. R. B., On the theoretical understanding of the unexpected O_2 activation by nanoporous gold. *Chem. Commun.* **2011,** *47* (29), 8403-8405.

17. Montemore, M. M.; Madix, R. J.; Kaxiras, E., How Does Nanoporous Gold Dissociate Molecular Oxygen? *J. Phys. Chem. C* **2016,** *120* (30), 16636-16640.

18. Krajčí, M.; Kameoka, S.; Tsai, A.-P., Understanding the catalytic activity of nanoporous gold: Role of twinning in fcc lattice. *J. Chem. Phys.* **2017,** *147* (4), 044713.

19. Moskaleva, L. V.; Weiss, T.; Klüner, T.; Bäumer, M., Chemisorbed Oxygen on the Au(321) Surface Alloyed with Silver: A First-Principles Investigation. *J. Phys. Chem. C* **2015,** *119* (17), 9215-9226.

20. Zugic, B.; Wang, L.; Heine, C.; Zakharov, D. N.; Lechner, B. A. J.; Stach, E. A.; Biener, J.; Salmeron, M.; Madix, R. J.; Friend, C. M., Dynamic restructuring drives catalytic activity on nanoporous gold-silver alloy catalysts. *Nat Mater* **2017,** *16* (5), 558-564.

21. Yan, M.; Jin, T.; Ishikawa, Y.; Minato, T.; Fujita, T.; Chen, L.-Y.; Bao, M.; Asao, N.; Chen, M.-W.; Yamamoto, Y., Nanoporous Gold Catalyst for Highly Selective Semihydrogenation of Alkynes: Remarkable Effect of Amine Additives. *J. Am. Chem. Soc.* **2012,** *134* (42), 17536-17542.

22. Wittstock, A.; Zielasek, V.; Biener, J.; Friend, C. M.; Bäumer, M., Nanoporous Gold Catalysts for Selective Gas-Phase Oxidative Coupling of Methanol at Low Temperature. *Science* **2010,** *327* (5963), 319.

23. Takale, B. S.; Feng, X.; Lu, Y.; Bao, M.; Jin, T.; Minato, T.; Yamamoto, Y., Unsupported Nanoporous Gold Catalyst for Chemoselective Hydrogenation Reactions under Low Pressure: Effect of Residual Silver on the Reaction. *J. Am. Chem. Soc.* **2016,** *138* (32), 10356-10364.

24. Wang, L.-C.; Personick, M. L.; Karakalos, S.; Fushimi, R.; Friend, C. M.; Madix, R. J., Active sites for methanol partial oxidation on nanoporous gold catalysts. *J Catal* **2016,** *344*, 778-783.

25. Biener, M. M.; Biener, J.; Wichmann, A.; Wittstock, A.; Baumann, T. F.; Bäumer, M.; Hamza, A. V., ALD Functionalized Nanoporous Gold: Thermal Stability, Mechanical Properties, and Catalytic Activity. *Nano Lett.* **2011,** *11* (8), 3085-3090.

26. Fujita, T.; Tokunaga, T.; Zhang, L.; Li, D.; Chen, L.; Arai, S.; Yamamoto, Y.; Hirata, A.; Tanaka, N.; Ding, Y.; Chen, M., Atomic Observation of Catalysis-Induced Nanopore Coarsening of Nanoporous Gold. *Nano Lett.* **2014,** *14* (3), 1172-1177.

27. Zugic, B.; Wang, L.; Heine, C.; Zakharov, D. N.; Lechner, B. A. J.; Stach, E. A.; Biener, J.; Salmeron, M.; Madix, R. J.; Friend, C. M., Dynamic restructuring drives catalytic activity on nanoporous gold-silver alloy catalysts. *Nat. Mater.* **2017,** *16* (5), 558-564.

28. Sun, Y.; Burger, S. A.; Balk, T. J., Controlled ligament coarsening in nanoporous gold by annealing in vacuum versus nitrogen. *Philosophical Magazine* **2014,** *94* (10), 1001-1011.

29. Biener, J.; Biener, M. M.; Nowitzki, T.; Hamza, A. V.; Friend, C. M.; Zielasek, V.; Bäumer, M., On the role of oxygen in stabilizing low-coordinated au atoms. *ChemPhysChem.* **2006,** *7* (9), 1906-1908.

30. Hoppe, S.; Li, Y.; Moskaleva, L. V.; Muller, S., How silver segregation stabilizes 1D surface gold oxide: a cluster expansion study combined with ab initio MD simulations. *Phys. Chem. Chem. Phys.* **2017,** *19* (22), 14845-14853.

31. Shi, H.; Stampfl, C., First-principles investigations of the structure and stability of oxygen adsorption and surface oxide formation at Au(111). *Phys. Rev. B* **2007,** *76* (7), 075327.

32. Landmann, M.; Rauls, E.; Schmidt, W. G., First-principles calculations of clean Au(110) surfaces and chemisorption of atomic oxygen. *Phys. Rev. B* **2009,** *79* (4), 045412.

33. Hiebel, F.; Montemore, M. M.; Kaxiras, E.; Friend, C. M., Direct visualization of quasi-ordered oxygen chain structures on Au(110)-(1 × 2). *Surf. Sci.*

34. Wichmann, A.; Wittstock, A.; Frank, K.; Biener, M. M.; Neumann, B.; Mädler, L.; Biener, J.; Rosenauer, A.; Bäumer, M., Maximizing Activity and Stability by Turning Gold Catalysis Upside Down: Oxide Particles on Nanoporous Gold. *ChemCatChem.* **2013,** *5* (7), 2037-2043.

35. Rodriguez, J. A.; Liu, P.; Graciani, J.; Senanayake, S. D.; Grinter, D. C.; Stacchiola, D.; Hrbek, J.; Fernández-Sanz, J., Inverse Oxide/Metal Catalysts in Fundamental Studies and Practical Applications: A Perspective of Recent Developments. *J. Phys. Chem. Lett.* **2016,** *7* (13), 2627-2639.

36. Bagge-Hansen, M.; Wichmann, A.; Wittstock, A.; Lee, J. R. I.; Ye, J.; Willey, T. M.; Kuntz, J. D.; van Buuren, T.; Biener, J.; Bäumer, M.; Biener, M. M., Quantitative Phase Composition of TiO_2-Coated Nanoporous Au Monoliths by X-ray Absorption Spectroscopy and Correlations to Catalytic Behavior. *J. Phys. Chem. C* **2014,** *118* (8), 4078-4084.

37. Rumancev, C.; von Gundlach, A. R.; Baier, S.; Wittstock, A.; Shi, J.; Benzi, F.; Senkbeil, T.; Stuhr, S.; Garamusx, V. M.; Grunwaldt, J. D.; Rosenhahn, A., Morphological analysis of cerium oxide stabilized nanoporous gold catalysts by soft X-ray ASAXS. *RSC Advances* **2017,** *7* (72), 45344-45350.

38. Palomino, R. M.; Gutiérrez, R. A.; Liu, Z.; Tenney, S.; Grinter, D. C.; Crumlin, E.; Waluyo, I.; Ramírez, P. J.; Rodriguez, J. A.; Senanayake, S. D., Inverse Catalysts for CO Oxidation: Enhanced Oxide–

Metal Interactions in MgO/Au(111), CeO_2/Au(111), and TiO_2/Au(111). *ACS Sustain. Chem. Eng.* **2017,** *5* (11), 10783-10791.

39. Ding, L.; Xiong, F.; Jin, Y.; Wang, Z.; Sun, G.; Huang, W., Surface reaction network of CO oxidation on CeO_2/Au(110) inverse model catalysts. *Phys. Chem. Chem. Phys.* **2016,** *18* (47), 32551-32559.

40. Rodriguez, J. A.; Ma, S.; Liu, P.; Hrbek, J.; Evans, J.; Pérez, M., Activity of CeO_x and TiO_x Nanoparticles Grown on Au(111) in the Water-Gas Shift Reaction. *Science* **2007,** *318* (5857), 1757-1760.

41. Shi, J.; Schaefer, A.; Wichmann, A.; Murshed, M. M.; Gesing, T. M.; Wittstock, A.; Bäumer, M., Nanoporous Gold-Supported Ceria for the Water–Gas Shift Reaction: UHV Inspired Design for Applied Catalysis. *J. Phys. Chem. C* **2014,** *118* (50), 29270-29277.

42. Shi, J.; Mahr, C.; Murshed, M. M.; Zielasek, V.; Rosenauer, A.; Gesing, T. M.; Bäumer, M.; Wittstock, A., A versatile sol–gel coating for mixed oxides on nanoporous gold and their application in the water gas shift reaction. *Catal. Sci. Technol.* **2016,** *6* (14), 5311-5319.

43. Shi, J.; Mahr, C.; Murshed, M. M.; Gesing, T. M.; Rosenauer, A.; Bäumer, M.; Wittstock, A., Steam reforming of methanol over oxide decorated nanoporous gold catalysts: a combined in situ FTIR and flow reactor study. *Phys. Chem. Chem. Phys.* **2017,** *19* (13), 8880-8888.

44. Kim, H. Y.; Henkelman, G., CO Oxidation at the Interface of Au Nanoclusters and the Stepped-CeO_2(111) Surface by the Mars–van Krevelen Mechanism. *J. Phys. Chem. Lett.* **2013,** *4* (1), 216-221.

45. Haruta, M.; Tsubota, S.; Ueda, A.; Sakurai, H., Synergism in the catalysis of supported gold. In *Stud. Surf. Sci. Catal.*, lnui, T.; Fujimoto, K.; Uchijima, T.; Masai, M., Eds. Elsevier: 1993; Vol. 77, pp 45-52.

46. Haruta, M., Spiers Memorial Lecture Role of perimeter interfaces in catalysis by gold nanoparticles. *Faraday Discuss.* **2011,** *152* (0), 11-32.

47. Wang, Y.-G.; Mei, D.; Glezakou, V.-A.; Li, J.; Rousseau, R., Dynamic formation of single-atom catalytic active sites on ceria-supported gold nanoparticles. *Nat. Commun.* **2015,** *6*, 6511.

48. Vilhelmsen, L. B.; Hammer, B., Identification of the Catalytic Site at the Interface Perimeter of Au Clusters on Rutile TiO_2(110). *ACS. Catal.* **2014,** *4* (6), 1626-1631.

49. Green, I. X.; Tang, W.; Neurock, M.; Yates, J. T., Insights into Catalytic Oxidation at the Au/TiO_2 Dual Perimeter Sites. *Acc. Chem. Res.* **2014,** *47* (3), 805-815.

50. Widmann, D.; Behm, R. J., Activation of Molecular Oxygen and the Nature of the Active Oxygen Species for CO Oxidation on Oxide Supported Au Catalysts. *Acc. Chem. Res.* **2014,** *47* (3), 740-749.

51. Zhang, C.; Michaelides, A.; Jenkins, S. J., Theory of gold on ceria. *Phys. Chem. Chem. Phys.* **2011,** *13* (1), 22-33.

52. Paier, J.; Penschke, C.; Sauer, J., Oxygen Defects and Surface Chemistry of Ceria: Quantum Chemical Studies Compared to Experiment. *Chem. Rev.* **2013,** *113* (6), 3949-3985.

53. Rodriguez, J. A., Gold-based catalysts for the water–gas shift reaction: Active sites and reaction mechanism. *Catal. Today* **2011,** *160* (1), 3-10.

54. Zhou, Z.; Kooi, S.; Flytzani-Stephanopoulos, M.; Saltsburg, H., The Role of the Interface in CO Oxidation on Au/CeO_2 Multilayer Nanotowers. *Adv. Funct. Mater.* **2008,** *18* (18), 2801-2807.

55. Longo, A.; Liotta, L. F.; Pantaleo, G.; Giannici, F.; Venezia, A. M.; Martorana, A., Structure of the Metal–Support Interface and Oxidation State of Gold Nanoparticles Supported on Ceria. *J. Phys. Chem. C* **2012,** *116* (4), 2960-2966.

56. Kim, H. Y.; Lee, H. M.; Henkelman, G., CO Oxidation Mechanism on CeO_2-Supported Au Nanoparticles. *J. Am. Chem. Soc.* **2012,** *134* (3), 1560-1570.

57. Wang, Y.-G.; Yoon, Y.; Glezakou, V.-A.; Li, J.; Rousseau, R., The Role of Reducible Oxide–Metal Cluster Charge Transfer in Catalytic Processes: New Insights on the Catalytic Mechanism of CO Oxidation on Au/TiO_2 from ab Initio Molecular Dynamics. *J. Am. Chem. Soc.* **2013,** *135* (29), 10673-10683.

58. Kim, H. Y.; Henkelman, G., CO Oxidation at the Interface between Doped CeO_2 and Supported Au Nanoclusters. *J. Phys. Chem. Lett.* **2012,** *3* (16), 2194-2199.

59. Duan, Z.; Henkelman, G., Calculations of CO Oxidation over a Au/TiO_2 Catalyst: A Study of Active Sites, Catalyst Deactivation, and Moisture Effects. *ACS. Catal.* **2018,** *8* (2), 1376-1383.

60. Molina, L. M.; Rasmussen, M. D.; Hammer, B., Adsorption of O_2 and oxidation of CO at Au nanoparticles supported by TiO_2(110). *J. Chem. Phys.* **2004,** *120* (16), 7673-7680.

61. Camellone, M. F.; Fabris, S., Reaction Mechanisms for the CO Oxidation on Au/CeO_2 Catalysts: Activity of Substitutional Au^{3+}/Au^{+} Cations and Deactivation of Supported Au^{+} Adatoms. *J. Am. Chem. Soc.* **2009,** *131* (30), 10473-10483.

62. Schlexer, P.; Widmann, D.; Behm, R. J.; Pacchioni, G., CO Oxidation on a Au/TiO_2 Nanoparticle Catalyst via the Au-Assisted Mars–van Krevelen Mechanism. *ACS. Catal.* **2018,** *8* (7), 6513-6525.

63. Migani, A.; Neyman, K. M.; Bromley, S. T., Octahedrality versus tetrahedrality in stoichiometric ceria nanoparticles. *Chem. Commun.* **2012,** *48* (35), 4199-4201.

64. Loschen, C.; Migani, A.; Bromley, S. T.; Illas, F.; Neyman, K. M., Density functional studies of model cerium oxide nanoparticles. *Phys. Chem. Chem. Phys.* **2008,** *10* (37), 5730-5738.

65. VandeVondele, J.; Krack, M.; Mohamed, F.; Parrinello, M.; Chassaing, T.; Hutter, J., Quickstep: Fast and accurate density functional calculations using a mixed Gaussian and plane waves approach. *Comput. Phys. Commun.* **2005,** *167* (2), 103-128.

66. Perdew, J. P., Density-functional approximation for the correlation energy of the inhomogeneous electron gas. *Phys. Rev. B* **1986,** *33* (12), 8822-8824.

67. Perdew, J. P.; Burke, K.; Ernzerhof, M., Generalized gradient approximation made simple. *Phys. Rev. Lett.* **1996,** *77* (18), 3865-3868.

68. Janthon, P.; Kozlov, S. M.; Viñes, F.; Limtrakul, J.; Illas, F., Establishing the Accuracy of Broadly Used Density Functionals in Describing Bulk Properties of Transition Metals. *J. Chem. Theory Comput.* **2013,** *9* (3), 1631-1640.

69. Janthon, P.; Luo, S.; Kozlov, S. M.; Viñes, F.; Limtrakul, J.; Truhlar, D. G.; Illas, F., Bulk Properties of Transition Metals: A Challenge for the Design of Universal Density Functionals. *J. Chem. Theory Comput.* **2014,** *10* (9), 3832-3839.

70. Grimme, S.; Antony, J.; Ehrlich, S.; Krieg, H., A consistent and accurate ab initio parametrization of density functional dispersion correction (DFT-D) for the 94 elements H-Pu. *J. Chem. Phys.* **2010,** *132* (15), 154104.

71. Lippert, G.; Michele, P.; Jurg, H., A hybrid Gaussian and plane wave density functional scheme. *Mol. Phys.* **1997,** *92* (3), 477-488.

72. VandeVondele, J.; Hutter, J., Gaussian basis sets for accurate calculations on molecular systems in gas and condensed phases. *J. Chem. Phys.* **2007,** *127* (11), 114105.

73. Goedecker, S.; Teter, M.; Hutter, J., Separable dual-space Gaussian pseudopotentials. *Phys. Rev. B* **1996,** *54* (3), 1703.

74. Nosé, S., A unified formulation of the constant temperature molecular dynamics methods. *J. Chem. Phys.* **1984,** *81* (1), 511-519.

75. Hoover, W. G., Canonical dynamics: equilibrium phase-space distributions. *Phys. Rev. A* **1985,** *31* (3), 1695.

76. Liu, J.-C.; Tang, Y.; Chang, C.-R.; Wang, Y.-G.; Li, J., Mechanistic Insights into Propene Epoxidation with O_2–H_2O Mixture on Au_7/α-Al_2O_3: A Hydroproxyl Pathway from ab Initio Molecular Dynamics Simulations. *ACS. Catal.* **2016,** *6* (4), 2525-2535.

77. Henkelman, G.; Jónsson, H., Improved tangent estimate in the nudged elastic band method for finding minimum energy paths and saddle points. *J. Chem. Phys.* **2000,** *113* (22), 9978-9985.

78. Chang, C.-R.; Yang, X.-F.; Long, B.; Li, J., A Water-Promoted Mechanism of Alcohol Oxidation on a Au(111) Surface: Understanding the Catalytic Behavior of Bulk Gold. *ACS. Catal.* **2013,** *3* (8), 1693-1699.

79. Song, W.; Hensen, E. J. M., A computational DFT study of CO oxidation on a Au nanorod supported on CeO_2(110): on the role of the support termination. *Catal. Sci. Technol.* **2013,** *3* (11), 3020-3029.

80. Hussain, A.; Curulla Ferré, D.; Gracia, J.; Nieuwenhuys, B. E.; Niemantsverdriet, J. W., DFT study of CO and NO adsorption on low index and stepped surfaces of gold. *Surf. Sci.* **2009,** *603* (17), 2734-2741.

81. Mehmood, F.; Kara, A.; Rahman, T. S.; Henry, C. R., Comparative study of CO adsorption on flat, stepped, and kinked Au surfaces using density functional theory. *Phys. Rev. B* **2009,** *79* (7), 075422.

82. Penschke, C.; Paier, J., Reduction and oxidation of Au adatoms on the CeO2(111) surface – DFT+U versus hybrid functionals. *Phys. Chem. Chem. Phys.* **2017,** *19* (19), 12546-12558.

83. Branda, M. M.; Castellani, N. J.; Grau-Crespo, R.; Leeuw, N. H. d.; Hernandez, N. C.; Sanz, J. F.; Neyman, K. M.; Illas, F., On the difficulties of present theoretical models to predict the oxidation state of atomic Au adsorbed on regular sites of CeO_2(111). *J. Chem. Phys.* **2009,** *131* (9), 094702.

84. Tosoni, S.; Pacchioni, G., Oxide-Supported Gold Clusters and Nanoparticles in Catalysis: A Computational Chemistry Perspective. *ChemCatChem.* **2019,** *11* (1), 73-89.